PHYSICAL REVIEW B **100**, 104404 (2019)

Thermal gradients and anomalous Nernst effects in membrane-supported nonlocal spin valves

R. K. Bennet, A. Hojem,[*] and B. L. Zink[†]
Department of Physics and Astronomy, University of Denver, Denver, Colorado 80208, USA

(Received 25 April 2019; revised manuscript received 14 August 2019; published 3 September 2019)

Metallic nonlocal spin valves (NLSVs) are important in modern spintronics due to their ability to separate pure spin current from charge current. These metallic nanostructures, often constructed from features with widths in the deep submicron regime, generate significant thermal gradients in operation, and the heat generated has important consequences for spin injection and transport. We use e-beam nanolithography to manufacture NLSVs with Ni-Fe alloy ferromagnetic nanowires and aluminum spin channels on 500-nm silicon nitride (Si-N) membranes to lower the thermal conductance of the substrate dramatically. While this extreme example of thermal engineering in a spintronic system increases the background nonlocal signals in ways expected based on earlier work, it also enhances thermoelectric effects, including the anomalous Nernst effect, and reveals a previously unknown thermally assisted electrical spin injection that results from a purely in-plane thermal gradient. We examine these effects as a function of temperature and, by careful comparison with 2D finite element models of the thermal gradients calculated at a single temperature, demonstrate that the anomalous Nernst coefficient of the 35-nm-thick Ni-Fe alloy, $R_\mathrm{N} = 0.17$ at $T = 200$ K, is in line with the few previous measurements of this effect for thin films.

DOI: 10.1103/PhysRevB.100.104404

I. INTRODUCTION

Nonlocal spin valves (NLSVs), also known as lateral spin valves or spin accumulation sensors, have emerged as an important part of modern spintronics thanks to their ability to separate pure spin current from charge current [1–5]. Industrial applications of NLSVs, such as hard-disk read heads, are rapidly approaching reality [6–10] .Therefore, it is important to quantify the effects of circuit size and material choice, as well as the nature of the injection mechanisms to produce sensors with sufficient signal-to-noise ratio for demanding applications [11–18]. Included in that list of materials is the substrate; for example, increasing the thermal conductance of the substrate reduces the background nonlocal resistance, which in turn affects the sensitivity of the NLSV sensor [19]. This is only one indication of the importance of thermal gradients in these nanoscale metallic circuits, as thermal and thermoelectric effects including the Seebeck, Peltier, and anomalous Nernst effects (ANE) are now understood to dominate the background nonlocal resistance [20–23], and at least contribute to the shape of switching signals. As shown in Fig. 1(a), the ANE is often interpreted as the thermoelectric analog to the anomalous Hall effect, where spin polarization of the electrons in a metallic ferromagnet combine with spin-dependent scattering and/or intrinsic Berry phase effects to produce a transverse electric field in response to a thermal gradient [24–29]. The electric field produced by the ANE, ∇V_N, is given by the equation

$$\nabla V_\mathrm{N} = -S_\mathrm{N}\widehat{m} \times \nabla T, \tag{1}$$

where $S_\mathrm{N} = R_\mathrm{N} S_\mathrm{FM}$ is the transverse Seebeck coefficient dependent on the absolute Seebeck coefficient S_FM and the anomalous Nernst coefficient R_N of the ferromagnetic material, $\widehat{m}$ is the unit vector in the direction of the magnetization of the ferromagnetic (FM) detector, and ∇T is the thermal gradient. Note that other representations for anomalous transverse thermoelectric effects are possible and may be used to emphasize particular relationships with other transport coefficients [29]. We chose the equation above for simple connection to the applied thermal gradient and relationship to the longitudinal Seebeck coefficient. Enhanced thermal gradients in the NLSV near the detector can generate voltage contributions that strongly affect the NLSV switching characteristics and, with the proper choice of magnetization orientation and current operating points, can increase the signal size in an NLSV sensor, though further study of how the thermal gradients can be engineered is required to take advantage of this effect. Thermal gradients at the crucial ferromagnet/nonmagnetic metal interface can also drive spin injection in the structure in what is often termed the spin-dependent Seebeck effect (SDSE) [30–39]. The dramatic consequences of the interaction of heat and spin place NLSVs firmly in the growing field of spin caloritronics [40–42] that examines coupling between heat and spin in materials and devices.

As shown in Fig. 2(a), the basic structure of the NLSV is two FM nanowires connected by a nonmagnetic (NM) channel, with the separation L between the FM wires on the order of the spin diffusion length λ_NM. Producing a spin accumulation in the channel is possible via two distinct methods. In the typical use of the NLSV, which we term electrical injection, we drive charge current from one FM through the interface and out the branch of the NM channel, away from the second FM. Spins that accumulate at the

---

[*] Present address: Department of Physics, University of California, San Diego, CA 92093.

[†] Corresponding author: barry.zink@du.edu

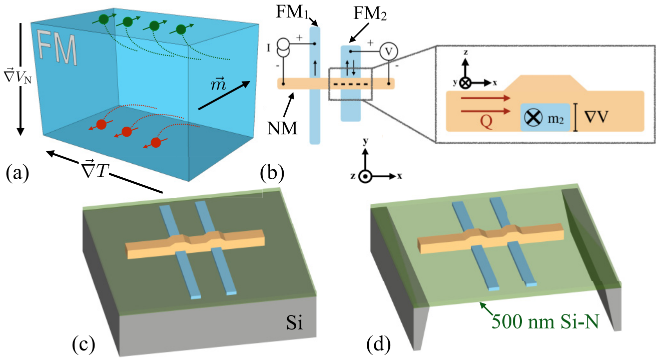

FIG. 1. (a) Cartoon illustration of the anomalous Nernst effect (ANE). A thermal gradient $\vec{\nabla}T$ applied to a metallic ferromagnet with magnetization $\vec{m}$ drives motion of spin-polarized electrons which experience either spin-dependent transverse scattering due to spin-orbit coupling or a transverse force generated by a spin-dependent Berry phase, generating an electric field $\vec{\nabla}V_N$. (b) A schematic view of the two FM nanowires bridged by a NM channel that form an NLSV with a cutaway cartoon showing the direction of the heat flow $\vec{Q}$ (and resulting thermal gradient), magnetization m_2, and resulting ANE electric field $\vec{\nabla}V$. (c), (d) Schematic view of NLSVs supported by a bulk substrate (c) and suspended on a 500-nm-thick Si-N membrane (d). Suspending the NLSV leads to dramatically different thermal gradients in and near the NLSV, since heat cannot escape directly to the bulk substrate.

injection contact diffuse in the NM channel, and the resulting difference in spin-dependent chemical potential contributes a spin-dependent component to the voltage, V_{nl}, measured at the opposite end of the NLSV, where no charge current flows. In what we term thermal injection, one FM is heated by the applied charge current, without explicitly driving current into the NM channel. This creates a thermal gradient at the FM/NM interface, which drives spin injection via the SDSE and similar spin diffusion and detection at the distant FM contact. Even in the electrical injection case, thermal effects play a significant role, since the often large charge current density flowing through the FM nanowire, across the interface, and then into the NM nanowire produces Joule heating of the nanoscale structure. The charge flow through these features also leads to heat flow through the Peltier effect. The thermal energy generated flows to the electrically insulating substrate, but must first be converted to vibrational, or phonon, energy. The flow of this heat energy from nanoscale metallic features to phonons in the substrate involves complicated physical processes that are not well understood for every combination of material constituents and feature size [43–47]. The combination of these effects creates potentially large and nontrivial thermal gradients in the NLSV structure. As a rough first step to discuss the consequences of this thermal profile, we assign labels to the average equilibrium spin injection and spin detection junction temperatures in the NLSV, T_{inj}, and T_{det}, as indicated in Figs. 2(b) and 2(c). Note also that the NLSV is usually produced with some degree of asymmetry in the size of the FM contacts, which can lead to different area and volume of the contact regions and different thermal profiles when the role of the contacts is switched, as shown in Figs. 2(g)–2(j). Even in cases where NLSVs are designed with symmetric junction areas [14], the additional volume of the FM required to assure distinct switching fields could introduce asymmetry in the thermal profile since the electron-phonon coupling in nanoscale features scales with the total volume of the system [48,49], and coupling to ballistic phonons varies with the area of a nanoscale metallic wire [45].

Thermoelectric and thermomagnetic effects convert this thermal profile into measurable signals in the NLSV that are independent of pure spin flow effects. Such nonspin signals are typically referred to as background nonlocal voltage or nonlocal resistance. For example, the NM and FM materials have absolute Seebeck coefficients S_{NM} and S_{FM}, respectively. The relative Seebeck coefficient relevant to the effective thermocouple of these two wires is then $S_{rel} = S_{NM} - S_{FM}$, and the elevated temperature of the detector junction leads to a voltage contribution to the NLSV signal,

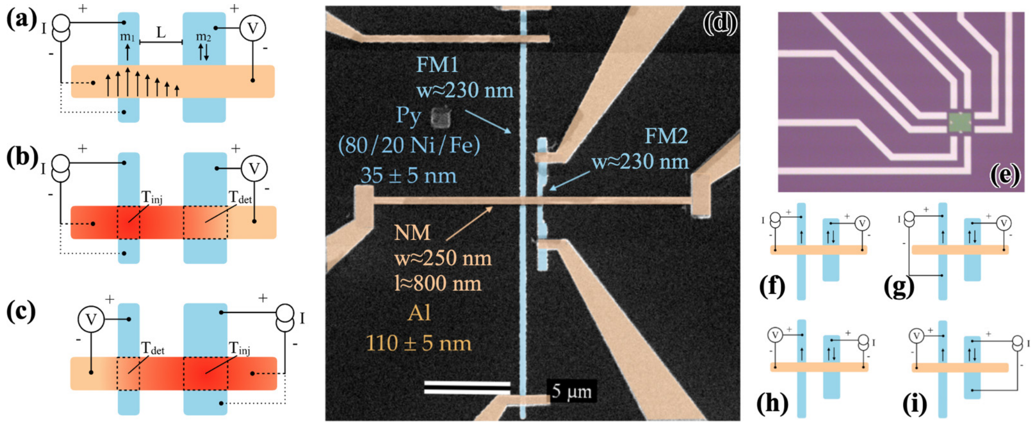

FIG. 2. (a) Top-view schematic of electrical (solid, dashed) and thermal (solid, dotted) spin injection and spin diffusion for NLSV in orientation A. Magnetizations m_1 and m_2, as well as separation length L are indicated. (b), (c) Schematic depiction of the heating of the NLSV in orientation A (b) and orientation B (c) The areas where we consider the average FM/NM junction temperatures T_{inj} and T_{det} are shown with dashed lines. (d) False-color scanning electron micrograph of a NLSV. Nominal channel widths and film thicknesses are given. (e) Optical micrograph of electrical leads surrounding a Si-N membrane (green). (f)–(i) Schematics of orientation A electrical (f) and thermal (g) injection, and orientation B electrical (h) and thermal (i) injection.

$\Delta V = S_{\rm rel}(T_{\rm det} - T_0)$, where T_0 is the bath temperature (typically assumed to be the temperature of the substrate far from the junction). The choice of the substrate material affects the phonon thermal conductance from the NLSV to the thermal bath and strongly affects $T_{\rm det}$ and the contribution to the background signal via ΔV. In addition to the Seebeck contribution that is determined ultimately by the average temperature differences in the NLSV, the ANE can contribute measurable voltages that depend on the thermal gradient near the detecting FM [21,23,38].

In this paper, we use micro- and nanofabrication techniques to alter the thermal profile in a typical NLSV dramatically. We fabricate the nanoscale metallic features on a suspended silicon-nitride (Si-N) membrane, which has very low thermal conductance. Aspects of the results provide clear confirmation of the previous understanding of thermal and thermoelectric effects in NLSVs, chiefly a dramatic increase in the NLSV background signal compared to devices fabricated on the same chip but supported by a bulk Si substrate. However, the dramatic change in thermal gradients reveals two effects not previously reported; an increase in the ANE portion of the signal that can enhance spin detection in the NLSV for properly chosen field conditions, and an enhancement of the spin transport following electrical spin injection due to the presence of a thermal gradient in the plane of the channel. Furthermore, the essentially 2D nature of the membrane greatly simplifies the heat flow in these NLSVs, allowing a higher degree of confidence in calculation of the thermal profile via finite element modeling. Use of such calculations allows us to determine a value for the ANE coefficient in the permalloy used for the FM contacts in these devices, which is in line with the few existing measurements of this quantity for thin-film and nanoscale FM features.

II. EXPERIMENT

Fabrication of the NLSV structures begins with a 500-μm -thick Si-N coated silicon wafer with prepatterned platinum electrical contacts for making contact with structures created by e-beam lithography. On the back side of the wafer, we use photolithography and plasma etching to pattern cleave marks for 1-cm square chips and windows in the Si-N that will form membranes. We then submerge the wafer into 60% TMAH held at 95 °C for 10 h to etch through the entire Si wafer. Each chip's design features six 90 μm × 90 μm square Si-N membrane windows and three substrate-supported areas, each with contacts and alignment features for e-beam lithography. This allows us to produce membrane and substrate devices on the same chip using the same deposition steps to minimize variations between devices. An example of the Pt electrical contacts surrounding a membrane structure is shown in Fig. 2(e).

On these chips, we fabricate NLSVs using permalloy (the Ni-Fe alloy with ~80% Ni, abbreviated Py) FM and aluminum NM via a two-step e-beam lithography liftoff process similar to that presented in earlier work [37]. The two FM nanowires are patterned with different shapes to create different switching fields. A scanning electron micrograph of this NLSV is shown in Fig. 2(d) with annotations detailing nominal geometries. As with the devices in our earlier work [37], these NLSVs are produced in a two-step fabrication process, and thus the FM layer forms a native oxide from exposure to atmosphere. We performed an Ar RF-cleaning step immediately prior to the deposition of the NM layer, but we do not believe this to be sufficient to remove the oxide. Our previous work shows that while this layer reduces observed signal size under electrical spin injection by loss of interfacial spin current polarization, it does not inhibit thermal spin injection [37].

TABLE I. Measured lateral geometries for all four devices described here, including widths of FM and NM channels and the separation distance between the injector and detector FM strips. All measurements are given in nm.

		FM 1	FM 2	Channel	Separation L
500 nm	Membrane	203 ± 12	413 ± 13	296 ± 10	481 ± 9
	Substrate	252 ± 39	391 ± 22	344 ± 21	459 ± 15
800 nm	Membrane	240 ± 30	240 ± 30	245 ± 30	760 ± 30
	Substrate	235 ± 30	235 ± 30	285 ± 30	770 ± 30

We produced two pairs of devices of two intended separations, $L = 500$ nm and $L = 800$ nm, on both membranes and substrates, on two different chips. Devices of different L are on different chips, but both chips had both the FM and NM layers deposited at the same time. The two separations use somewhat different shapes for FM2, with the $L = 800$ nm NLSVs using a shape with a narrow midsection [as shown in Fig. 2(d)], while the $L = 500$ nm NLSVs use a simpler wide rectangle with designed width of 400 nm as shown in our previous work [37]. Both metal layers are produced via e-beam evaporation, the Py layer at ≈0.1 nm/s in a load-locked UHV chamber with typical base pressure $\ll 10^{-8}$ Torr, and the Al layer in a high vacuum chamber at a higher rate ≈0.5 − 1 nm/s.

The Si-N membranes are not only insulating, but also electrically and optically transparent. This has advantages and challenges for e-beam lithography. One resulting challenge is a difficulty in focusing the SEM onto the membrane structure itself for e-beam lithography. However, the membranes are small enough that they do not buckle, allowing for lithography optimization performed on the substrate to be sufficient for our needs. An advantage of the electron transparency of the membrane is that no secondary electrons can be generated in the bulk substrate, and this reduces a source of broadening of the exposed line in the e-beam resist. This potentially allows narrower features in the resulting liftoff on the membrane. In any given NLSV, these competing effects of improved intrinsic resolution and quality of beam optimization can cause unpredictable lateral size of the final structures. To understand any resulting variations in signal size, we measured the completed NLSVs after fabrication and testing using an SEM and present the results in Table I. For the $L = 500$ nm membrane, NLSV, the width of FM1, and the channel are closer to the intended design width than seen in the corresponding NLSVs on the substrate, with smaller standard errors in the geometry measurements. The wider FM2 does not show this clear advantage from lithography on the membrane, and this drives a variation in the separation length, L. For the $L = 800$ nm membrane NLSV, the FM widths are similar and near the designed width for both substrate and membrane devices, but the channel width is much closer to the design in the membrane device.

Measurements of the channel and contact resistance for the $L = 500$ nm NLSVs also suggest possibly helpful effects of growth and fabrication of the membrane. Measurements on these two NLSVs at 78 K show extremely linear channel IV curves that, together with the geometric variations shown above, give charge resistivities $\rho_{\mathrm{Al}} = 6.6\ \mu\Omega$ cm for the membrane NLSV and $\rho_{\mathrm{Al}} = 10.9\ \mu\Omega$ cm for the substrate NLSV. Three-wire contact resistance measurements, described in more detail elsewhere [37], are both negative values for low bias currents, but lower for the membrane than the substrate ($R_{\mathrm{cont}} = -5$ mΩ for the membrane and -30 mΩ for the substrate, both measured at 78 K). These values suggest that during the RF cleaning of the FM and subsequent growth of the Al channel, higher temperatures develop because of the thermal isolation from the membrane, and that this could lead to cleaner interfaces and somewhat larger Al grains.

All transport measurements use the same experimental apparatus and methodology detailed in previous work, using the "delta mode" feature of the Keithley 2128a nanovoltmeter for resistance measurements and numerically integrated differential conductance curves for measurements of IV characteristics [37]. In the following, we denote the "delta mode" nonlocal resistance measurements, which functionally integrate the nonlocal resistance contributions that are odd in applied I, as R with no subscript to distinguish from the fit coefficients of the IV curve.

III. RESULTS

Figures 1(a) and 1(b) illustrate how the ANE generates voltages in an NLSV. Heat, Q, generated by the charge current through the injector FM produces an in-plane thermal gradient, ∇T, perpendicular to the magnetization, m. This generates a voltage at the detector due to the spin polarization of the FM. To first order, no charge current flows near the detector junction, so the voltages we observe arise only from the ANE and do not have components from transverse Peltier effects. The resulting ANE signal can be seen in the R vs H switching characteristic of the NLSV, where $R = V/I$ is the nonlocal resistance. Figure 3(a) is a schematic view of an NLSV with ANE contributions, which add the typical shape of the FM hysteresis loop to the usual pattern that is even in H. As a result, the maximum H points, where the FM strips are aligned in parallel, have different electric potential as the direction of ∇T is set by the location of the heated charge current injection site. The difference between these positive H and negative H points with parallel FM strips, labeled P_{p} and P_{n}, respectively, is then $2V_{\mathrm{N}}$. The intermediate field points where only one FM has switched to align with the reversing H, AP_{p}, and AP_{n}, are also modified. Depending on the choice of operating points that are compared, the nonlocal voltage difference will either represent the typical pure spin-current effects or add $2V_{\mathrm{N}}$, as clarified in Fig. 4. Note that these patterns depend on the direction of the in-plane thermal gradient that drives the ANE, which reverses when the detector and injector FM are reversed. This is demonstrated in Fig. 3(d), using R vs H measured at 300 K for a membrane-supported NLSV with $L = 500$ nm. Since $V_{\mathrm{N}} \propto S_{\mathrm{N}} \propto S_{\mathrm{FM}}$, and since the Seebeck coefficient for metals is roughly proportional to T, the ANE should be larger at higher temperatures, and is very likely to contribute to practical NLSV sensors.

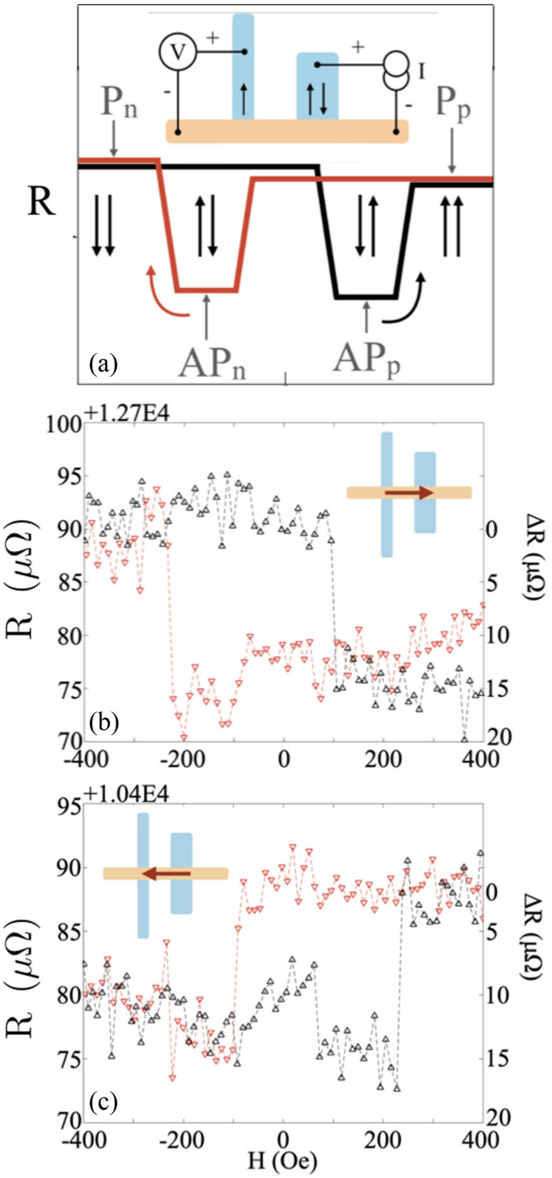

FIG. 3. (a) Schematic illustration of a typical R vs H sweep demonstrating ANE. The relative locations of the parallel-positive (P_{p}), parallel-negative (P_{n}), antiparallel-positive (AP_p), and antiparallel-negative (AP_n) are labeled for orientation A. (b), (c) R vs H sweeps for 500-nm membrane-supported devices in orientation A (b) and orientation B (c) at 300 K. The slightly different heating conditions have a small difference in background nonlocal R, indicated here by the different shifts of the y axis applied to each (given above each plot). Insets illustrate the direction of heat flow across the device for each orientation.

Figure 4 clarifies the expected pattern of switching seen in the NLSV when the traditional spin-current signal is added to the ANE developed in response to an in-plane thermal

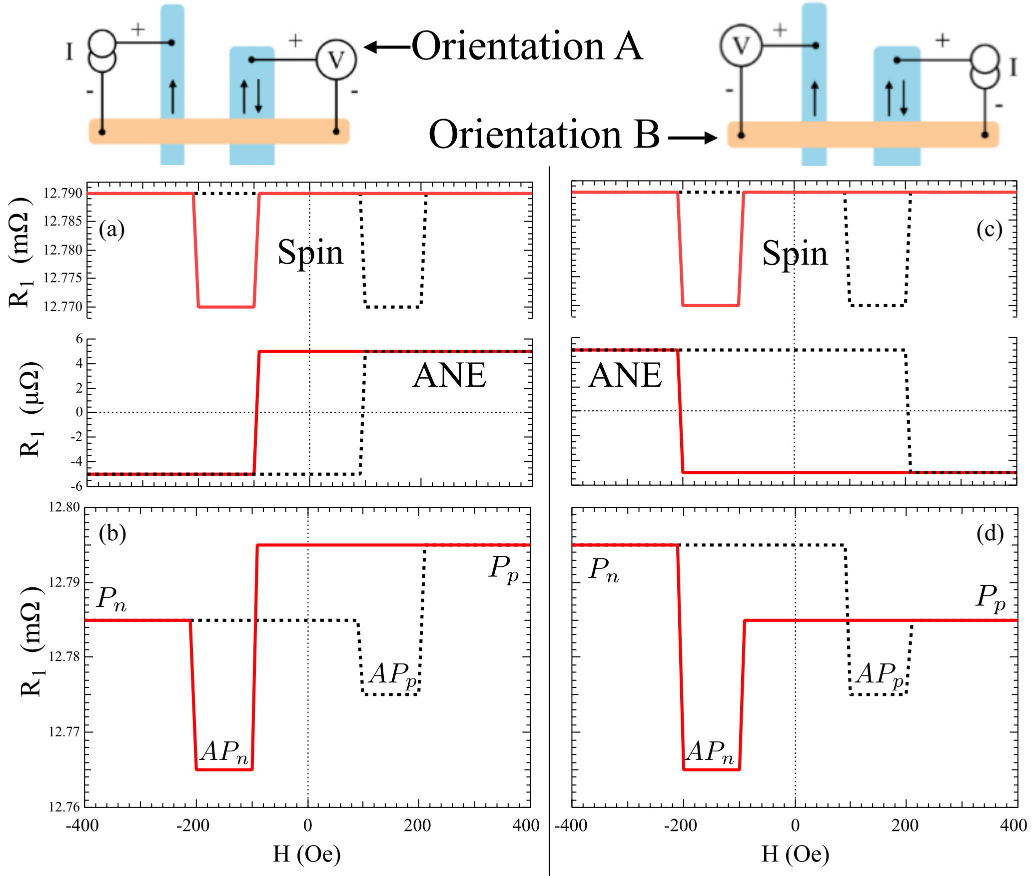

Orientation	W/O ANE	With ANE
A	$P_p - AP_p$ $P_n - AP_n$	$P_p - AP_n$ $P_n - AP_p$

Orientation	W/O ANE	With ANE
B	$P_p - AP_n$ $P_n - AP_p$	$P_p - AP_p$ $P_n - AP_n$

FIG. 4. (a), (c) Examples of pure spin (top) and ANE (bottom) R vs H for orientation A (a) and orientation B (c). (b), (d) The resulting expected total R vs H for orientation A (b) and orientation B (d). The table at the bottom lists the IV curve subtractions used to isolate the signals with and without ANE for both orientations.

gradient present at the detector. Figures 4(a) and 4(c) schematically show the two signal components separately for orientations A and B, and Figs. 4(b) and 4(d) the resulting total nonlocal resistance. Switching the role of the FM strips from injector to detector has two consequences. First, the reversed thermal gradient switches the sign of the ANE voltage component as demanded by the symmetry of Eq. (1). Second, the coercive field of the ANE component changes since this is physically tied to the switching field of the detector FM, which is the lower (higher) H_c strip in orientation A (B). The contributions of the two different signal components can be isolated from the total response using the comparisons listed in the tables below each pattern in Fig. 4.

As in our earlier and other work [37,38], we use the nonlocal resistance R vs H measurements to identify the four switching locations of the NLSV, then measure the nonlocal voltage as a function of applied current at values of H given at the bottom of Fig. 4. This allows us to isolate contributions from the various thermal effects. For background (raw) data, we examine the IV curves at full saturation (±400 Oe; P_p or P_n, respectively); spin and ANE data is isolated by subtracting IV curves. Through appropriate choice of IV-curve subtractions, we may choose to isolate spin signals without including ANE, or include the ANE component as part of the overall spin signal.

An example of the raw IV curves taken at the parallel-negative point ($P_\mathrm{n} = -400$ Oe) and the subtracted IV curves excluding ANE is shown for orientation A in Fig. 5. Here, subtracted ($V_{\mathrm{nl,spin}}$) IV curves ($P_\mathrm{n} - AP_\mathrm{n}$) remove both the background signal and the ANE signal and isolate the other spin effects. Although the spin signals are on the same order of magnitude, the membrane-supported devices show much larger raw IV signals than the substrate-supported devices. Since background effects have large contributions from thermoelectric effects, the larger background suggests a larger $T_{\mathrm{det}} - T_0$, which is a very reasonable result of thermally isolating the NLSV on the membrane. The strongly parabolic nonlocal voltages, even in the nominally electrically driven spin injection configuration, are clear evidence of thermal effects caused by Joule heating and have been observed by several groups on substrate-supported NLSVs [19,22,23,37]. When the NLSV is more thermally isolated using the membrane, the background becomes much larger, and higher-order nonlinearities become obvious whether the NLSV is operated in electrical injection configuration, Fig. 5(a), or in thermal injection configuration, Fig. 5(c).

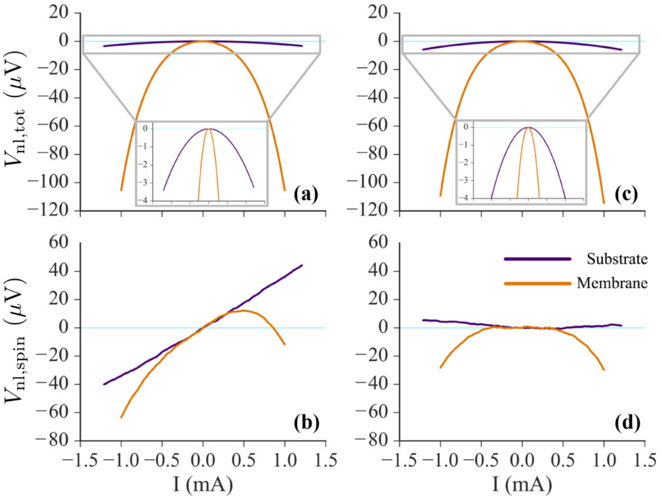

FIG. 5. Raw ($V_{\mathrm{nl,tot}}$) and subtracted ($V_{\mathrm{nl,spin}}$) *IV* curves for the 800-nm membrane and substrate devices in orientation A at a bath temperature of 78 K for both electrical (a), (b) and thermal (c), (d) spin injection. Subtracted *IV* curves ($P_{\mathrm{n}} - AP_{\mathrm{n}}$) isolate the spin signal from the background as well as from ANE that is included in the raw *IV* curves. The membrane devices show consistently larger signals.

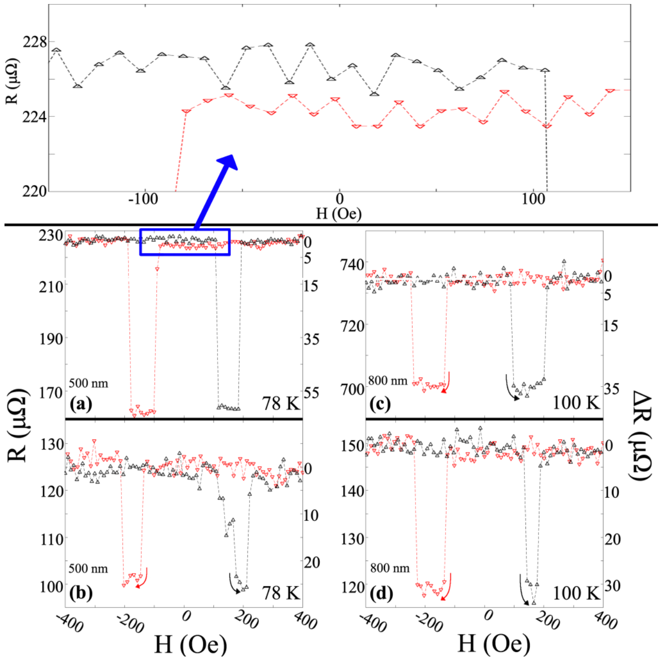

FIG. 6. *R* vs *H* for 500-nm (a), (b) and 800-nm (c), (d) membrane-supported (a), (c) and substrate-supported (b), (d) devices in orientation B at bath temperatures of 78 K and 100 K, respectively. Here, ΔR corresponds to the R_1 fit coefficient value. The top plot shows a closer view of the highlighted region in (a) with clear ANE compared to the 800-nm membrane-supported device and to both substrate-supported devices.

Since V_{nl} is overwhelmingly nonlinear, especially in the membrane devices, we use a polynomial expansion $V_{nl} = R_1 I + R_2 I^2 + \ldots$ to fit the *IV* curves. Peltier heating is proportional to *I*, while Joule heating is proportional to I^2; thus, for the background signal, R_1 and R_2 are the fit coefficients corresponding to Peltier and Joule heating, respectively. Higher-order terms most likely arise due to the temperature dependence of the resistivity, Seebeck, and/or Peltier coefficients of the metals forming the NLSV.

Figure 6 plots the nonlocal resistance, *R*, vs applied magnetic field *H* for four NLSVs in orientation B: two fabricated on Si-N membranes [Figs. 6(a) and 6(c)] and two with the same designed FM separation fabricated at the same time but supported by a bulk Si substrate beneath the Si-N layer [Figs. 6(b) and 6(d)]. At the moderately low temperatures used here (100 K or below), a signal component with the symmetry of the ANE is visible only in the membrane-supported device with $L = 500$ nm, where there is a difference in *R* between the up- and down-sweeps between $H = -100$ Oe and $H = 100$ Oe. This ANE signal is notably absent in the substrate-supported device with the same separation. The reduction in the spin-signal component with increasing *L* for the two membrane-supported devices, from $\Delta R \simeq 70\ \mu\Omega$ at $L = 500$ nm to $\Delta R \simeq 30\ \mu\Omega$ at $L = 800$ nm, is consistent with the single-exponential drop we observed on substrate-supported NLSVs fabricated using the same deposition techniques reported earlier [37]. Here we observe that the substrate-supported $L = 800$ nm device has very similar ΔR to the membrane-supported device, while for the $L = 500$ nm devices, the substrate-supported NLSV has roughly half the spin signal. Though we cannot definitively rule out that the thermal isolation plays a role, calculation of the expected signal based on the full 1D model of spin transport presented by Takahashi and Maekawa [50], taking into account the measured geometry and ρ_{Al} of each device, predicts nearly exactly such a drop in spin signal for the $L = 500$ nm substrate-supported device. In the case of the membrane device, the small, negative three-terminal contact resistance suggests that the simplified model of transparent FM/NM contacts is appropriate. Assuming values for the bulk spin polarization of the permalloy, $\alpha = 0.35$; the spin diffusion length of the Py, $\lambda_{\mathrm{FM}} = 3.5$ nm; and of the NM, $\lambda_{\mathrm{Al}} = 760$ nm; which were observed in our previous work on similar NLSVs and are well within typical ranges, gives a predicted spin signal of $R_1 \approx 75\ \mu\Omega$. The larger negative contact resistance of the $L = 500$ nm substrate device suggests the full model with no simplifications is the best description, though the difference between the full model and the transparent model is minimal for the likely parameters of this device. Both models predict a spin signal of $R_1 \approx 25\ \mu\Omega$ at 78 K. These model predictions are very much in line with the observed results.

Figure 7 compares the spin-signal components for the two $L = 500$ nm devices as a function of the bath temperature of the NLSV for orientation A under electrical spin injection. These are determined from subtracted *IV* curves for selected applied field. The signal proportional to *I*, R_1, is shown in Figs. 7(a) and 7(b), and that proportional to I^2, R_2, in Figs. 7(c) and 7(d). Typically, the R_1 term is interpreted as an electrically driven spin component, and the R_2 term is interpreted as a thermally driven spin component since Joule heating is $\propto I^2$. We have chosen subtractions to isolate the spin signal (using field points $P_p - AP_p$ and $P_n - AP_n$) and ANE component ($P_p - P_n$) for this orientation. The R_1 component of the spin

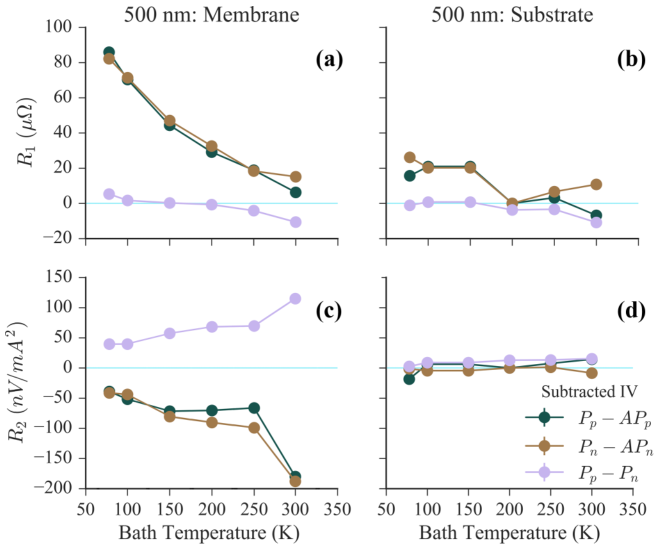

FIG. 7. R_1 (a), (b) and R_2 (c), (d) vs bath temperature for 500-nm membrane and substrate devices in orientation A, electrical injection. Here, $P_p - AP_p$ and $P_n - AP_n$ represent simultaneous determinations of the isolated spin resistance without ANE; the $P_p - P_n$ curve represents twice the ANE signal produced by the devices. Note that both the ANE and the spin-resistance signals are significantly larger in the membrane devices than the substrate devices, particularly at low temperatures.

signal shows the drop between the membrane and substrate devices driven by geometry and channel resistivity explained above, along with the typical drop of R_1 with increasing temperature seen in NLSVs. R_1 also shows a small ANE component prominent only at larger temperatures, where the Seebeck and Nernst coefficients become large. We clarify that this represents the appearance of the ANE, which requires generation of a thermal gradient, in the term purely linear with applied I, rather than the I^2 term tied to Joule heating. The thermal gradient that drives this ANE term is therefore odd with respect to I, and we believe is generated by the Peltier heating/cooling that occurs at the FM injector/NM channel interface. The extreme thermal isolation of the Si-N membrane allows this additional Peltier power term to generate a thermal gradient at the distant detector contact.

The spin signal components when thermally driven [Figs. 7(c) and 7(d)] show trends that are distinctly different from the electrical case. The ANE component in the membrane device [the purple symbols in Fig. 7(c)] is large, and also increases with T as expected for the ANE. The spin component of R_2 also becomes large for the membrane device. In a typical NLSV, this would be viewed as evidence of the SDSE, though here we note that the membrane allows a large *in-plane* thermal gradient, but does not support the out-of-plane thermal gradient required for the SDSE. For the substrate-supported NLSV, both R_2 terms are dramatically smaller. We explore this unique form of thermally assisted spin transport further in Sec. IV A below.

The trends in the ANE signal component are borne out by the data in Fig. 8. Here we plot $R_{2,\mathrm{ANE}} = [R_2(P_p) - R_2(P_n)]/2$ vs T, to give the clearest view of ANE contributions for all four NLSVs in both electrical and thermal spin injection. In all panels, orange symbols represent data on membrane-supported NLSVs and purple symbols represent substrate-supported NLSVs. The $L = 800$ nm membrane-supported device failed before reliable data could be collected at all six temperatures. Figure 8(a) shows ANE contributions to

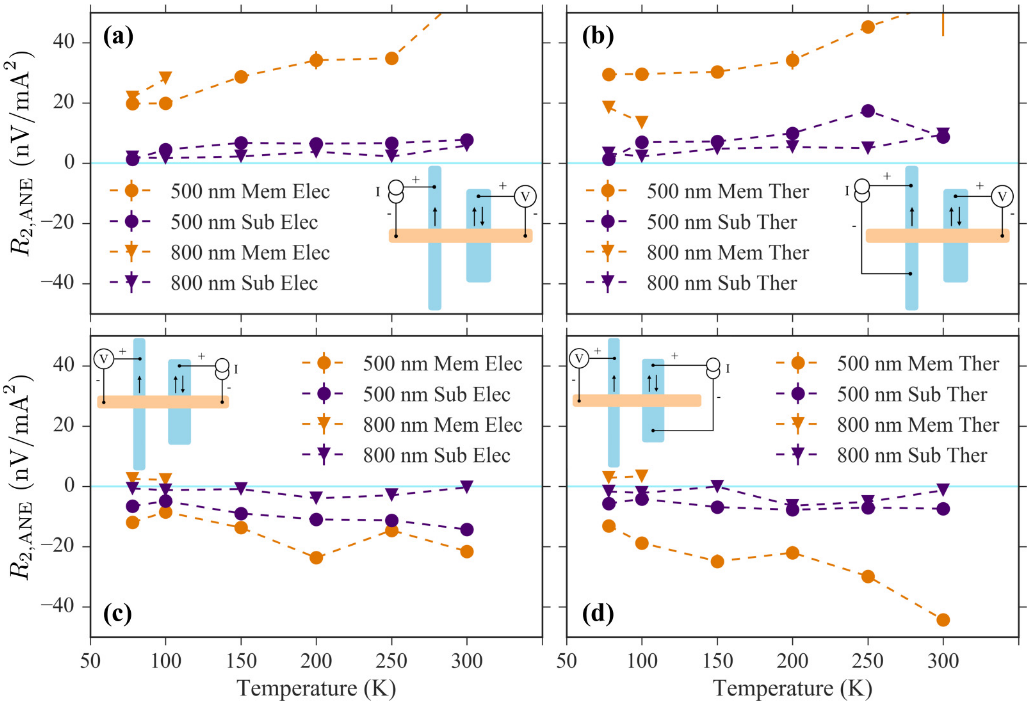

FIG. 8. $R_{2,\mathrm{ANE}}$ vs T for $L = 500$ nm and $L = 800$ nm membrane- and substrate-supported devices in electrical (a), (c) and thermal (b), (d) spin injections for orientation A (a), (b) and orientation B (c), (d).

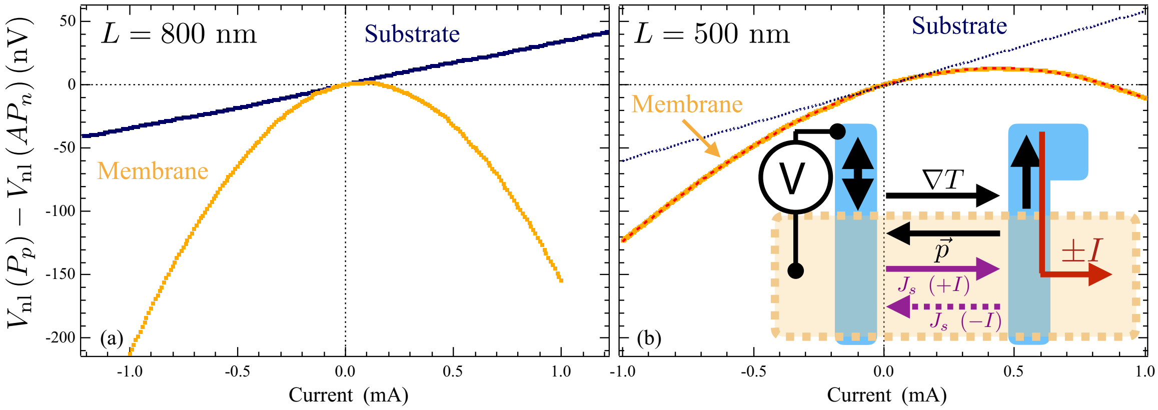

FIG. 9. $V_{\rm nl}(P_p) - V_{\rm nl}(AP_n)$ vs I for NLSVs in orientation B using electrical spin injection at 78 K. (a) Direct comparison of spin-isolated (ANE removed) IV curves for the $L = 800$ nm substrate (blue symbols) and membrane (orange symbols) NLSVs. The large in-plane thermal gradient in the membrane device drives an additional spin signal $\propto I^2$. (b) A similar plot compares the membrane-supported $L = 500$ nm NLSV to the predicted linear term for a more closely matched substrate-supported NLSV (blue dotted line). Inset: A schematic view of the charge current, $\pm I$, spin current $\pm J_s$ (with direction in the channel dependent on the polarity of I), thermal gradient ΔT, and the average phonon momentum, $\vec{p}$.

electrical spin injection in orientation A, where the membrane-supported NLSVs have ∼10× higher ANE signals throughout the temperature range due to the large in-plane thermal gradients. The narrower 500-nm separation between the FM contacts also increases the magnitude of the thermal gradient compared to the 800-nm separation, which in turn increases the magnitude of the ANE. The result of reversing the thermal gradient by using orientation B shown in Fig. 8(b) gives approximately the same magnitude of signal with a reversed sign, again in agreement with the symmetry of the ANE. The magnitudes are slightly different in this orientation, which we attribute to the difference in geometry of the FM contacts. Figures 8(b) and 8(d) show ANE contributions under thermal spin injection in orientations A and B, respectively. These show not only the same patterns as in electrical injection, with large signals on membrane-supported NLSVs where a larger in-plane thermal gradient develops, but nearly the same magnitude of the ANE components. This very reasonably supports the view that the ANE component depends on the presence, size, and direction of the thermal gradient at the detector, and is independent of the nature of the injection that caused the heat flow.

IV. DISCUSSION

A. Thermally assisted spin transport on membranes

In Fig. 9, we more closely examine the thermally assisted spin transport effect seen in Figs. 5(b) and 7(c). Here, we show $V_{\rm nl}(P_p) - V_{\rm nl}(AP_n)$ vs bias current I for the membrane- and substrate-supported NLSVs in orientation B using electrical spin injection at 78 K. This subtraction isolates effects due to spin current flow and explicitly excludes ANE. For both the $L = 800$ nm [Fig. 9(a)] and $L = 500$ nm [Fig. 9(b)] NLSVs, this IV curve shows a very strong term $\propto I^2$, which is typically attributed to Joule heating. For the case of the $L =$ 800 nm NLSV, we compare this IV curve directly to its analog for the substrate-supported device, which shows only the linear dependence normally dominant in electrical injection. The reduction in the electrical spin signal driven by the different geometry and ρ_{Al} for the $L = 500$ nm substrate-supported NLSV prevents the direct comparison; so in Fig. 9(b), we compare the membrane NLSV curve to the curve that would be generated in an NLSV with the same R_1 term but no thermal term. The red dashed line shows the curve fit to terms linear and quadratic in I used to determine R_1. Following the example of the $L = 800$ nm pair, we assume that a better-matched NLSV would have no significant R_2 term, though this comparison is only for illustration. In both curves, the I^2 heat-driven term is large and opposite in sign to the typical electrical spin injection signal, such that at a moderate positive current, the sign of the spin-isolated nonlocal voltage reverses, indicating that the spin current flow in the NM channel has reversed direction.

We propose that this reversal of the spin current flow is driven by a direct interaction between the spin current flow and the phonon flux in the NM channel driven by the in-plane gradient set up in the membrane-supported NLSV. The relevant charge, spin, heat, and phonon momentum flow directions are indicated schematically in the inset to Fig. 9(b). Here, ∇T points at the charge injector site, which is predominantly where heat is generated in the structure. The resulting flow of phonons away from this site generates a transfer of momentum $\vec{p}$ that exists throughout the NM channel. When this momentum opposes the flow of spin current J_s, the spin current is first reduced in magnitude, stopped (near $I = 0.85$ mA for the $L = 500$ nm NLSV), and eventually reversed in direction. For the opposite sign of applied charge current, the spin current and phonon momentum point in the same direction, such that the generation of the in-plane thermal gradient always assists the spin current flow.

To our knowledge, this direct interaction of a pure spin current with the phonon flow associated with an in-plane thermal gradient in a NM metal has not been previously considered or observed. We clarify that this signal cannot arise due to the SDSE, as the tiny thermal mass of the Si-N membrane reduces any ability of the structure to support significant heat flow in the direction perpendicular to the FM/NM interface as occurs when the interface is supported by the comparably huge bulk substrate. We also note that the magnitude of the R_2 terms seen here are very large compared to those we explained via the SDSE in similar NLSVs [37], which showed $R_2 \simeq -16$ nV/mA^2. Thermally assisted electrical spin injection has been reported [22,31], albeit in substrate-supported NLSVs where this effect is most likely driven by the same physics as the SDSE, which relies on presence of a thermal gradient in the FM near the FM/NM interface. A potentially similar mechanism for thermally driven spin current in a NM channel of a nonlocal spin valve was recently proposed for experiments on graphene [51], which though not suspended, could develop a significant in-plane thermal gradient due to the extreme difference in thermal conductance between the 2D graphene layer and the supporting substrate.

B. Thermal modeling and determination of ANE coefficient

To provide context for both the thermally driven NM channel spin transport and the generation of signals by the ANE in these devices, we now consider the temperature profile generated in the membrane-supported NLSV devices in greater detail. Before applying more complicated computational methods, we first make a rough estimation of the temperatures generated in the membrane-supported NLSVs. Since the background V_{nl} is dominated by a Seebeck voltage, we estimate the maximum ΔT simply by assuming that $V_{\mathrm{nl,tot}} = S_{\mathrm{rel}}\Delta T$, where $S_{\mathrm{rel}} = S_{\mathrm{Py}} - S_{\mathrm{Al}} \sim 3\ \mu\mathrm{V/K}$ as we reported previously for similar NLSVs [37]. The substrate-supported $L = 500$ nm device shows $V_{\mathrm{nl,tot}} \sim -3\ \mu$V at $I = 1$ mA, which suggests $\Delta T = T_{\mathrm{det}} - T_0 \sim 1$ K. The much larger $V_{\mathrm{nl,tot}}$ in the membrane-supported case suggests much higher temperatures are generated, with the same simple estimate suggesting $\Delta T = T_{\mathrm{det}} - T_0$ more than 30× higher at $T_0 = 78$ K, though there are two problems with this approach. First, ignoring the higher-order nonlinearity in the background V_{nl} at large I potentially overestimates the temperature generated. Second, as discussed in greater detail below, much more of the electrical path of the detector branch of the NLSV circuit is heated. This introduces additional thermoelectric voltages that are important to consider not only for determining T, but also for correct estimation of the ANE coefficient.

For a more accurate estimate of the thermal gradients generated in the membrane-supported NLSV, we perform 2D finite element calculations of the heat flow in the device. The removal of the bulk substrate and resulting near-2D confinement of the thermal gradient in the membrane structure allows us to use this simple approach to characterize temperature gradients in membrane-supported NLSVs. Calculations of this sort have been previously used to model temperature profiles in micro- and nanocalorimeters supported on Si-N membranes that are very similar to the suspended NLSV [52–55]. Using a commercially available software package [56], we solved the 2D heat flow equation in steady state,

$$\frac{\partial}{\partial x}\left(k_{2\mathrm{D}}(x,y)\frac{\partial T(x,y)}{\partial x}\right) + \frac{\partial}{\partial y}\left(k_{2\mathrm{D}}(x,y)\frac{\partial T(x,y)}{\partial y}\right) = P_{2\mathrm{D}}(x,y), \tag{2}$$

where $k_{2\mathrm{D}} = k \cdot t$ with k the thermal conductivity (in W/mK) of the NLSV components and t the thickness of the films. As for our previous work [37], values of the thermal conductivities were calculated from the Wiedemann-Franz law with values of L informed by measurements of the thermal conductivity of similar films made with micromachined thermal isolation platforms. At $T = 200$ K, this gives $k_{\mathrm{Al}} = 47$ W/mK and $k_{\mathrm{Py}} = 20$ W/mK [57]. We take values for Si-N from our previous measurements of thermal conductivity [58,59], which indicate $k \sim 3$W/mK near 200 K. We focus on the thermal injection geometry, as this avoids the complication of adding Peltier heating and cooling to the injector FM/NM junction, and also keep the modeled current in the regime that avoids higher-order nonlinearity. We set $P_{2\mathrm{D}}$ dissipated in the FM for thermal spin injection based on the applied current $I = 0.274$ mA and the resistance of the structure.

We present results of this model for the membrane-supported NLSV at a base temperature of 200 K in Fig. 10. The temperature profile, shown for the entire NLSV [Fig. 10(a)] indicates a roughly symmetric heated region at the center of the NLSV membrane that rises by 14 K even for this relatively modest applied current. A closer view of the active region of the NLSV shown in Fig. 10(b) indicates the hot spot remains largely symmetric in the y direction, though is not uniform near the more highly conductive NM channel, as expected. Though the thermal gradients are highest in the membrane due to its very low thermal conductivity, significant gradients still exist in the various metallic structures of the NLSV. We also note that elevated T exists across the entire detector FM. In the membrane-supported case, this has the important consequence that the background response is formed from two thermocouples, rather than a simple single thermocouple raised to an elevated temperature at the FM/NM detector junction. This makes the background dependent on the temperature difference between the typical detector junction (where the right-hand FM contacts the NM channel), and the intersection of the larger Al lead with the FM near the top of the detector strip. The thermoelectric circuit path for the detector is shown by the dotted line in Fig. 10(c), with the two local temperatures, $T_{\mathrm{det,t}}$ and $T_{\mathrm{det,b}}$, indicated. The total thermoelectric background voltage generated across the detector is then

$$V_{\mathrm{nl}} = S_{\mathrm{Al}}(T_{\mathrm{det,b}} - T_0) + S_{\mathrm{Py}}(T_{\mathrm{det,t}} - T_{\mathrm{det,b}}) + S_{\mathrm{Al}}(T_0 - T_{\mathrm{det,t}}), \tag{3}$$

such that

$$V_{\mathrm{nl}} = (S_{\mathrm{Al}} - S_{\mathrm{Py}})(T_{\mathrm{det,b}} - T_{\mathrm{det,t}}) = S_{\mathrm{rel}}(T_{\mathrm{det,b}} - T_{\mathrm{det,t}}). \tag{4}$$

Using the calculated T values as shown in Fig. 10 and $S_{\mathrm{rel}} \sim -12\ \mu\mathrm{V/K}$, we estimate a background V_{nl} for the membrane NLSV at 200 K of ≈5 μV for $I = 0.274$ mA, which is very much in line with the measured background V_{nl} as shown in Fig. 5(c).

We determine the in-plane thermal gradient across the detector, ∇T_x, from the simulation results by plotting the temperature profile vs the x coordinate in the region near the detector at the y-coordinate location of the center of the NM channel. We show plots of this temperature profile in Figs. 10(e) and 10(f) for the bottom and top contacts, respectively. Though there is some slight nonlinearity in this profile, we estimate the thermal gradient with a linear fit to the T vs x data in this region, as indicated by the dark green

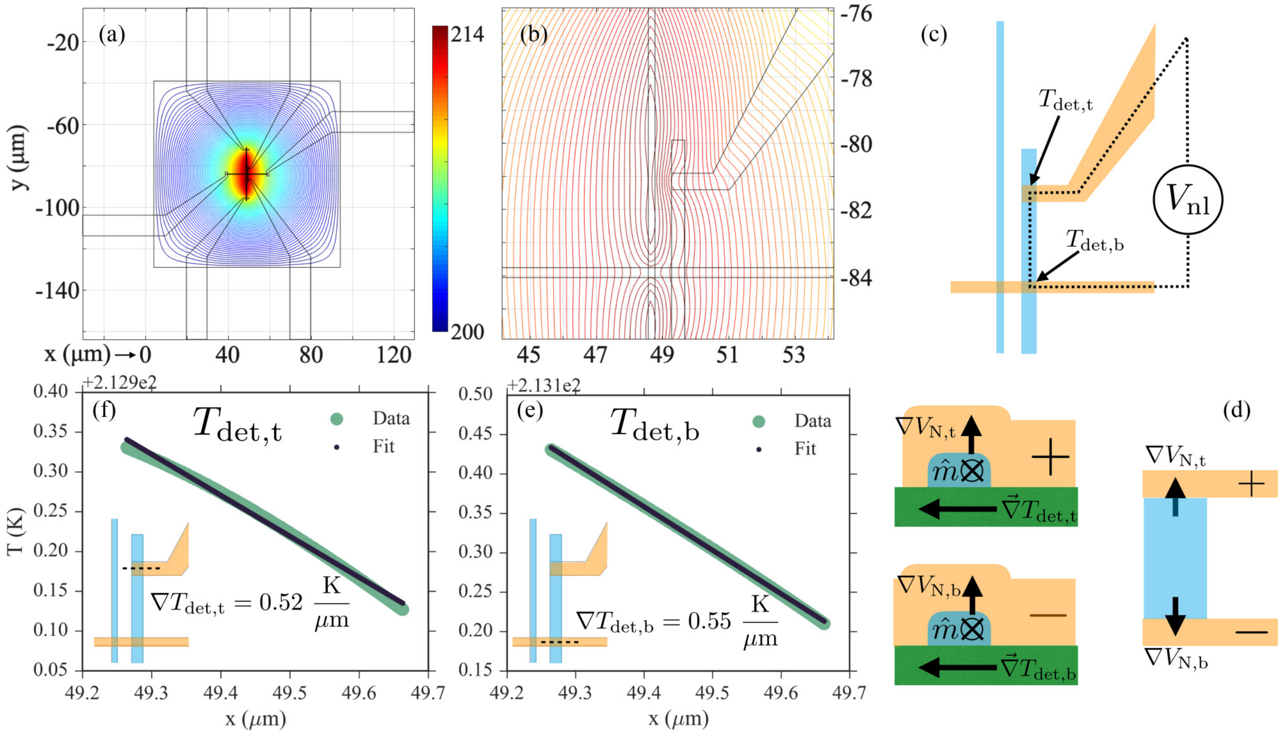

FIG. 10. 2D finite element modeling of the $L = 500$ nm membrane-supported NLSV in orientation A, thermal injection, shows the local temperature as a function of position across the entire membrane (a) and near the two injection siites (b). We detect V_{nl} through the NM channel and the patterned AL near the top of the detector FM. Thermal gradients at these two junctions, shown schematically in panel (c), reach temperatures $T_{\mathrm{det,t}}$ and $T_{\mathrm{det,b}}$ each generate electric field ∇V_{N} due to the ANE. However, the overall detected V_{N} is the difference of these contributions due to the definition of the current path. (e) and (f) show calculated values of $T_{\mathrm{det,t}}$ and $T_{\mathrm{det,b}}$, with linear fits used to determine the local gradient.

line. The resulting thermal gradients are shown in the relevant figures.

For a typical substrate-supported NLSV, integrating Eq. (1) for the geometry of the NLSV gives an expression for the ANE coefficient, R_N,

$$R_{\mathrm{N,substrate}} = -\frac{V_{\mathrm{ANE}}}{S_{\mathrm{Py}} \nabla T_x t_{Py}}, \tag{5}$$

where S_{Py} is the absolute Seebeck coefficient of the permalloy FM detector strip, t_{Py} is its thickness, and V_{ANE} is the voltage generated by the ANE. However, the significant heating of the entire detector branch shown in Fig. 10(b) demands more careful consideration. Since the ANE does not involve spin current effects, which we expect only near the NM channel, any location where an in-plane thermal gradient exists across the detector FM and the overlapping Al contact allows the resulting out-of-plane electric field to drive current along the Al lead and contribute a voltage that will be detected in V_{nl}. As shown schematically in Fig. 10(d), this occurs at two locations in the detector voltage measurement path in our experiments. As was the case with the thermoelectric voltage, the Nernst signal becomes dependent on the difference in the in-plane gradients at these two locations, rather than the total gradient generated at only one junction. Although $\nabla T_{\mathrm{det,b}}$, $\nabla T_{\mathrm{det,t}}$, $\hat{m}$, and the resulting Nernst electric fields all point in the same direction, the two electric fields point in opposite sense with respect to the measurement circuit, since (for the choice of $\hat{m}$ shown in Fig. 10(d)] $\vec{\nabla} V_{\mathrm{det,t}}$ points in the direction toward the defined positive contact while $\vec{\nabla} V_{\mathrm{det,b}}$ points toward the *negative* contact. In the membrane geometry, then

$$R_{\mathrm{N,membrane}} = -\frac{V_{\mathrm{ANE}}}{S_{\mathrm{Py}} t_{Py} (\nabla T_{\mathrm{det,b}} - \nabla T_{\mathrm{det,t}})}. \tag{6}$$

For the modeled conditions we use $R_{2,\mathrm{ANE}}$ from Fig. 8 and calculate

$$V_{\mathrm{ANE}} = [R_{2,\mathrm{ANE}}(200\ \mathrm{K})](0.274\ \mathrm{mA})^2.$$

From previous work with thermal isolation platforms developed by our laboratory for measuring thermopower [60], we find $S_{Py} = -12\mu V/K$ at a bath temperature of 200 K. The resulting estimate for thermal spin injection at 200 K is $R_{\mathrm{N}} = 0.17$, which is in good agreement with other values reported for permalloy ($R_{\mathrm{N}} = 0.13$ [21] and $R_{\mathrm{N}} = 0.2$ [25]). As is true for the Seebeck coefficient, the value of R_{N} is likely somewhat dependent on the nature of the scattering mechanisms present in a given sample, so some spread in reported values is sensible.

Finally, we note that the effects we have observed, including increased backgrounds, large ANE components, and potentially thermally assisted spin transport in the spin channel, are not unique to NLSVs fabricated on membranes, but could arise in any case where the balance of the thermal gradients generated in the nanoscale device tips from predominantly out-of-plane to more significant in-plane components. We expect the results presented here could inform other structures with more unusual thermal properties. These could range from all-epitaxial metallic NLSVs where the high degree of order could place a stronger emphasis on heat conduction across interfaces that could alter thermal profiles, to graphene, and other 2D systems with exceptionally high thermal conductivity and potentially poor coupling to supporting substrates [51,61].

V. CONCLUSION

In summary, we presented results of electrical and thermal spin injection as a function of temperature for both thermally isolated metallic NLSVs and similar structures supported by bulk substrates. The dramatically different heat sinking of the nanoscale devices between the two constructions leads to several observations that clarify the thermal physics of spin generation and transport in metallic structures. The thermal isolation generates larger temperatures in the NLSVs, which lead to larger backgrounds via thermoelectric effects that are largely understood. The generation of larger in-plane gradients in the membrane-supported NLSVs leads to larger signal components from the ANE, which exemplifies the role these magnetothermoelectric effects play in NLSVs.

ANEs are enhanced by the near-2D geometry, as demonstrated by the consistent increase in R_2 fit coefficients to the isolated ANE *IV* curves for membrane-supported devices over substrate-supported devices at the same separation and orientation. Thermally assisted electrical spin injection also appears in the membrane-supported devices, as demonstrated through the nonlinearity of the isolated spin *IV* curves. This effect is independent of the ANE, since we have excluded the ANE from these *IV* curves with our choice of subtractions. Additionally, these thin 500-nm Si-N membranes can be treated as nearly 2D, as shown by the good agreement of our calculated R_N values for the 500-nm membrane-supported device with values from previous works.

ACKNOWLEDGMENTS

We thank D. Wesenberg for assistance and advice on fabrication techniques and finite element calculations, and gratefully acknowledge support from the NSF (No. ECCS-1610904). This work was performed, in part, at the Center for Integrated Nanotechnologies, an Office of Science User Facility operated for the US Department of Energy (DOE) Office of Science by Los Alamos National Laboratory (Contract No. DE-AC52-06NA25396) and Sandia National Laboratories (Contract No. DE-AC04-94AL85000).

---

[1] M. Johnson, Phys. Rev. Lett. **70**, 2142 (1993).
[2] F. Jedema, A. Filip, and B. van Wees, Nature (London) **410**, 345 (2001).
[3] Y. Ji, A. Hoffmann, J. S. Jiang, and S. D. Bader, Appl. Phys. Lett. **85**, 6218 (2004).
[4] S. O. Valenzuela and M. Tinkham, Appl. Phys. Lett. **85**, 5914 (2004).
[5] Y. Niimi, D. Wei, H. Idzuchi, T. Wakamura, T. Kato, and Y. C. Otani, Phys. Rev. Lett. **110**, 016805 (2013).
[6] T. Nakatani, Z. Gao, and K. Hono, MRS Bull. **43**, 106 (2018).
[7] M. Erekhinsky, A. Sharoni, F. Casanova, and I. K. Schuller, Appl. Phys. Lett. **96**, 022513 (2010).
[8] Y. K. Takahashi, S. Kasai, S. Hirayama, S. Mitani, and K. Hono, Appl. Phys. Lett. **100**, 052405 (2012).
[9] M. Yamada, D. Sato, N. Yoshida, M. Sato, K. Meguro, and S. Ogawa, IEEE Trans. Magn. **49**, 713 (2013).
[10] A. Vedyayev, N. Ryzhanova, N. Strelkov, T. Andrianov, A. Lobachev, and B. Dieny, Phys. Rev. Appl. **10**, 064047 (2018).
[11] J. D. Watts, J. S. Jeong, L. O'Brien, K. A. Mkhoyan, P. A. Crowell, and C. Leighton, Appl. Phys. Lett. **110**, 222407 (2017).
[12] L. O'Brien, D. Spivak, J. S. Jeong, K. A. Mkhoyan, P. A. Crowell, and C. Leighton, Phys. Rev. B **93**, 014413 (2016).
[13] W. Yan, L. C. Phillips, M. Barbone, S. J. Hämäläinen, A. Lombardo, M. Ghidini, X. Moya, F. Maccherozzi, S. van Dijken, S. S. Dhesi, A. C. Ferrari, and N. D. Mathur, Phys. Rev. Lett. **117**, 147201 (2016).
[14] L. O'Brien, M. J. Erickson, D. Spivak, H. Ambaye, R. J. Goyette, V. Lauter, P. A. Crowell, and C. Leighton, Nat. Commun. **5**, 3927 (2014).
[15] N. Tombros, C. Jozsa, M. Popinciuc, H. T. Jonkman, and B. J. van Wees, Nature **448**, 571 (2007).
[16] X. Lou, C. Adelmann, S. A. Crooker, E. S. Garlid, J. Zhang, K. S. M. Reddy, S. D. Flexner, C. J. Palmstrom, and P. A. Crowell, Nat. Phys. **3**, 197 (2007).
[17] T. Kimura and Y. Otani, J. Phys.: Condens. Matter **19**, 165216 (2007).
[18] J. Hamrle, T. Kimura, Y. Otani, K. Tsukagoshi, and Y. Aoyagi, Phys. Rev. B **71**, 094402 (2005).
[19] S. Kasai, S. Hirayama, Y. K. Takahashi, S. Mitani, K. Hono, H. Adachi, J. Ieda, and S. Maekawa, Appl. Phys. Lett. **104**, 162410 (2014).
[20] F. L. Bakker, A. Slachter, J.-P. Adam, and B. J. van Wees, Phys. Rev. Lett. **105**, 136601 (2010).
[21] A. Slachter, F. L. Bakker, and B. J. van Wees, Phys. Rev. B **84**, 020412(R) (2011).
[22] F. Casanova, A. Sharoni, M. Erekhinsky, and I. K. Schuller, Phys. Rev. B **79**, 184415 (2009).
[23] S. Hu and T. Kimura, Phys. Rev. B **87**, 014424 (2013).
[24] T. Seki, R. Iguchi, K. Takanashi, and K. Uchida, J. Phys. D: Appl. Phys. **51**, 254001 (2018).
[25] T. C. Chuang, P. L. Su, P. H. Wu, and S. Y. Huang, Phys. Rev. B **96**, 174406 (2017).
[26] N. Nagaosa, J. Sinova, S. Onoda, A. H. MacDonald, and N. P. Ong, Rev. Mod. Phys. **82**, 1539 (2010).
[27] K. Behnia, J. Phys.: Condens. Matter **21**, 113101 (2009).
[28] Y. Pu, D. Chiba, F. Matsukura, H. Ohno, and J. Shi, Phys. Rev. Lett. **101**, 117208 (2008).
[29] T. Miyasato, N. Abe, T. Fujii, A. Asamitsu, S. Onoda, Y. Onose, N. Nagaosa, and Y. Tokura, Phys. Rev. Lett. **99**, 086602 (2007).

[30] A. Slachter, F. L. Bakker, J.-P. Adam, and B. J. van Wees, Nat. Phys. **6**, 879 (2010).

[31] M. Erekhinsky, F. Casanova, I. K. Schuller, and A. Sharoni, Appl. Phys. Lett. **100**, 212401 (2012).

[32] S. Hu, H. Itoh, and T. Kimura, NPG Asia Mater. **6**, e127 (2014).

[33] S. Hu and T. Kimura, Phys. Rev. B **90**, 134412 (2014).

[34] K. Yamasaki, S. Oki, S. Yamada, T. Kanashima, and K. Hamaya, Appl. Phys. Express **8**, 043003 (2015).

[35] A. Pfeiffer, S. Hu, R. M. Reeve, A. Kronenberg, M. Jourdan, T. Kimura, and M. Klaui, Appl. Phys. Lett. **107**, 082401 (2015).

[36] G.-M. Choi, C.-H. Moon, B.-C. Min, K.-J. Lee, and D. G. Cahill, Nat. Phys. **11**, 576 (2015).

[37] A. Hojem, D. Wesenberg, and B. L. Zink, Phys. Rev. B **94**, 024426 (2016).

[38] S. Hu, X. Cui, T. Nomura, T. Min, and T. Kimura, Phys. Rev. B **95**, 100403(R) (2017).

[39] S. Hu, J. Zhao, L. Wang, X. Cui, K. Ohnishi, T. Ariki, T. Min, K. Xia, and T. Kimura, Phys. Rev. Mater. **2**, 104403 (2018).

[40] G. E. W. Bauer, E. Saitoh, and B. J. van Wees, Nat. Mater. **11**, 391 (2012).

[41] S. R. Boona, R. C. Myers, and J. P. Heremans, Energy Environ. Sci. **7**, 885 (2014).

[42] C. H. Back, G. E. W. Bauer, and B. L. Zink, J. Phys. D: Appl. Phys. **52**, 230301 (2019).

[43] K. T. Regner, J. P. Freedman, and J. A. Malen, Nanoscale Microscale Thermophys. Eng. **19**, 183 (2015).

[44] D. G. Cahill, P. V. Braun, G. Chen, D. R. Clarke, S. Fan, K. E. Goodson, P. Keblinski, W. P. King, G. D. Mahan, A. Majumdar, H. J. Maris, S. R. Phillpot, E. Pop, and L. Shi, Appl. Phys. Rev. **1**, 011305 (2014).

[45] M. E. Siemens, Q. Li, R. Yang, K. A. Nelson, E. H. Anderson, M. M. Murnane, and H. C. Kapteyn, Nat. Mater. **9**, 26 (2010).

[46] E. Pop, Nano Res. **3**, 147 (2010).

[47] D. G. Cahill, W. K. Ford, K. E. Goodson, G. D. Mahan, A. Majumdar, H. J. Maris, R. Merlin, and S. R. Phillpot, J. Appl. Phys. **93**, 793 (2003).

[48] F. C. Wellstood, C. Urbina, and J. Clarke, Phys. Rev. B **49**, 5942 (1994).

[49] J. T. Karvonen, L. J. Taskinen, and I. J. Maasilta, Phys. Rev. B **72**, 012302 (2005).

[50] S. Takahashi and S. Maekawa, Phys. Rev. B **67**, 052409 (2003).

[51] J. F. Sierra, I. Neumann, J. Cuppens, B. Raes, M. V. Costache, and S. O. Valenzuela, Nat. Nanotechnol. **13**, 107 (2017).

[52] W.-J. Lee, H. J. Kim, J. W. Kim, D. H. Nam, K.-Y. Choi, and K. H. Kim, Thermochim. Acta **603**, 244 (2015), chip Calorimetry.

[53] C. Baldasseroni, D. R. Queen, D. W. Cooke, K. Maize, A. Shakouri, and F. Hellman, Rev. Sci. Instrum. **82**, 093904 (2011).

[54] Y. Anahory, M. Guihard, D. Smeets, R. Karmouch, F. Schiettekatte, P. Vasseur, P. Desjardins, L. Hu, L. Allen, E. Leon-Gutierrez, and J. Rodriguez-Viejo, Thermochim. Acta **510**, 126 (2010).

[55] B. Revaz, B. L. Zink, D. O'Neil, L. Hull, and F. Hellman, Rev. Sci. Instrum. **74**, 4389 (2003).

[56] MATLAB and Partial Differential Equations Toolbox Release 2018a, The MathWorks, Inc., Natick, Mass, USA.

[57] A. D. Avery, S. J. Mason, D. Bassett, D. Wesenberg, and B. L. Zink, Phys. Rev. B **92**, 214410 (2015).

[58] R. Sultan, A. D. Avery, J. M. Underwood, S. J. Mason, D. Bassett, and B. L. Zink, Phys. Rev. B **87**, 214305 (2013).

[59] R. Sultan, A. D. Avery, G. Stiehl, and B. L. Zink, J. Appl. Phys. **105**, 043501 (2009).

[60] A. D. Avery, R. Sultan, D. Bassett, D. Wei, and B. L. Zink, Phys. Rev. B **83**, 100401(R) (2011).

[61] A. L. Friedman, K. M. McCreary, J. T. Robinson, O. M. van 't Erve, and B. T. Jonker, Carbon **131**, 18 (2018).